CrossMark

uGMRT Observations of a Fast and Blue Optical Transient—AT 2018cow

Nayana A. J.[1,2] and Poonam Chandra[2]

[1] Department of physics, United Arab Emirates University, Al-Ain, 15551, UAE; nayan89deva@gmail.com
[2] National Centre for Radio Astrophysics, Tata Institute of Fundamental Research, P.O. Box 3, Pune, 411007, India
Received 2020 May 27; revised 2021 March 9; accepted 2021 March 9; published 2021 April 30

Abstract

We present low-fRequency radio observations of a fast-rising blue optical transient (FBOT), AT 2018cow, with the upgraded Giant Metrewave Radio Telescope (uGMRT). Our observations span $t = 11$–570 days post-explosion and a frequency range of 250–1450 MHz. The uGMRT light curves are best modeled as synchrotron emission from an inhomogeneous radio-emitting region expanding into an ionized medium. However, due to the lack of information on the source covering factor, which is a measure of the degree of inhomogeneity, we derive various parameters assuming the source covering factor to be unity. These parameters, hence, indicate limits on the actual values in an inhomogeneous model. We derive the lower limit of the shock radius to be $R \sim (6.1-14.4) \times 10^{16}$ cm at $t = 138-257$ days post-explosion. We find that the fast-moving ejecta from the explosion are moving with velocity $v > 0.2c$ up to $t = 257$ days post-explosion. The upper limits of the mass-loss rate of the progenitor are $\dot{M} \sim (4.1-1.7) \times 10^{-6}\ M_\odot\ \mathrm{yr}^{-1}$ at $(19.3-45.7)$ years before the explosion for a wind velocity $v_w = 1000$ km s^{-1}. These $\dot{M}$ values are ~ 100 times smaller than the previously reported mass-loss rate 2.2 years before the explosion, indicating an enhanced phase of the mass-loss event close to the end-of-life of the progenitor. Our results are in line with the speculation of the presence of a dense circumstellar shell in the vicinity of AT 2018cow from previous radio, ultra-violet, and optical observations.

Unified Astronomy Thesaurus concepts: Radio transient sources (2008); Circumstellar matter (241); Non-thermal radiation sources (1119)

1. Introduction

Fast blue optical transients (FBOTs) are a class of transients characterized by high optical luminosity ($\geqslant 10^{43}$ erg s^{-1}), fast rise time ($t < 12$ days), and blue colors (Drout et al. 2014; Rest et al. 2018). The observational properties of all FBOTs are not in-line with traditional supernova models (Drout et al. 2014; Pursiainen et al. 2018; Rest et al. 2018). The high peak luminosity and rapid rise time of FBOTs are difficult to explain with the radioactive decay of ^{56}Ni unless a very large Ni mass is assumed (Drout et al. 2014). There exist two categories of models in the literature to explain the energy of FBOTs, which is not due to radioactive decay. One is the interaction of the explosion shock with the surrounding medium (Balberg & Loeb 2011; Chevalier & Irwin 2011; Ginzburg & Balberg 2014) and the other is the power supplied by a central compact object (Yu et al. 2013; Metzger & Piro 2014; Hotokezaka et al. 2017). A detailed study of the properties of FBOTs as a group is limited because of the small number of known FBOTs, which is due to the low discovery rate.

AT 2018cow was discovered on 2018 June 16.44 UT (Smartt et al. 2018) with the Asteroid Terrestrial-Impact Last Alert System (ATLAS; Tonry et al. 2018) in the dwarf star-forming galaxy CGCG 137−068 at a distance of 66 Mpc (Prentice et al. 2018). The source was not detected by the All Sky Automatic Survey for Supernovae (ASAS-SN) on 2018 June 15.14 UT (Prentice et al. 2018), tightly constraining the time of the event. We assume 2018 June 16.44 UT to be the time of the event ($t = 0$) and all times (t) are mentioned with respect to this time throughout the paper.

AT 2018cow has been classified as an FBOT (Perley et al. 2019) and is the first FBOT detected in the local universe. Other than AT 2018cow there are only two FBOTs for which detailed multiwavelength follow-up observations exist; CSS161010

(Coppejans et al. 2020) and ZTF18abvkwla (Ho et al. 2020). AT 2018cow displayed several peculiar characteristics in its early evolutionary phase: rapid rise to peak ($t_{\mathrm{peak}} \leqslant 3$ days; Fremling 2018; Prentice et al. 2018), high peak optical luminosity ($L_{\mathrm{peak}} \sim 10^{44}$ erg s^{-1}) followed by a relatively fast decay ($t^{-2.5}$; Perley et al. 2019), initially featureless optical spectrum followed by broad short-lived spectral features (Perley et al. 2019; Prentice et al. 2018; Margutti et al. 2019), luminous and variable X-ray emission (Margutti et al. 2019) and bright submillimeter radio emission (Ho et al. 2019). Radio emission was detected from AT 2018cow at various frequencies from 1.4 GHz (Nayana & Chandra 2018) to 34 GHz (Dobie et al. 2018; Margutti et al. 2019) including very long baseline interferometry (VLBI) observations (Mohan et al. 2020; Bietenholz et al. 2020). There exist various progenitor scenarios in the literature attempting to explain the observed properties of AT 2018cow. These include stellar collapse leading to a compact object like a black hole or magnetar (Margutti et al. 2019), a tidal disruption event (TDE; Perley et al. 2019), a merger of two white dwarfs (Lyutikov & Toonen 2019), a jet driven by the collision of an accreting neutron star and a star (Soker et al. 2019), a failed explosion of a blue supergiant (Margutti et al. 2019), and an explosion of a luminous blue variable to an inhomogeneous CSM (Rivera Sandoval et al. 2018).

Regardless of the actual nature of the explosion, the radio emission from AT 2018cow is understood to be from the fastest ejecta interacting with the surrounding medium (Ho et al. 2019; Margutti et al. 2019). Ho et al. (2019) derived a shock velocity of $v \sim 0.13c$ in a medium of density $n_e = 3 \times 10^5$ cm^{-3} from early (up to day 81) submillimeter observations. The authors invoke a model in which the transient explodes in a dense CSM shell of radius $\sim 1.7 \times 10^{16}$ cm to explain multiepoch radio observations. Margutti et al. (2019) presented multifrequency Karl G. Jansky Very Large Array (JVLA) observations of

AT 2018cow during $t = 82$–150 days and model the radio emission as coming from a shock of velocity $v = 0.1c$ interacting with a dense environment. While the early radio observations probe the density and shock properties in the immediate vicinity of the transient, low-frequency observations at late times trace the environmental properties at larger radii.

We present the lowest frequency radio observations of AT 2018cow, carried out with the upgraded Giant Metrewave Radio telescope (uGMRT) covering a frequency range of $\sim$250–1450 MHz during 11−570 days post-explosion. We explain the uGMRT observations and data reduction in Section 2. The radio light curves and modeling are presented in Section 3. The properties of the shock and mass-loss rate of the progenitor are inferred in Section 4. We compare the properties of AT 2018cow with other energetic transients in Section 5 and summarize our results in Section 6.

2. UGMRT Observations and Data Reduction

We carried out uGMRT observations of AT 2018cow from 2018 June 27.8 ($t = 11$ days) until 2020 January 7.1 ($t = 570$ days). The observations were carried out in the uGMRT band 5 (1050−1450 MHz), band 4 (550−950 MHz), and band 3 (250−500) MHz. The data were recorded in 2048 frequency channels covering a bandwidth of 400 MHz in the bands 5 and 4 and 200 MHz in the band 3 with an integration time of 10 seconds in the total intensity mode. 3C286, 3C147, and 3C48 were used as the flux density and bandpass calibrators. The data were analyzed using the Common Astronomy Software Application package (CASA; McMullin et al. 2007). The data were flagged and calibrated using standard CASA tasks. The calibrated visibility data were imaged using CASA task TCLEAN. A few rounds of phase only self-calibration were performed to improve the image quality. The source flux density and errors are determined by fitting a two-dimensional Gaussian to the emission using the GAUSSFIT[3] tab available in CASA region manager panel. The free parameters of the fit are position angle, center, and major and minor axes of the Gaussian. The dimensions of the fitted Gaussian are consistent with a point source at all three frequency bands. The details of uGMRT observations and flux densities at central frequencies 1.25, 0.75, and 0.40 GHz in bands 5, 4, and 3, respectively, are presented in Table 1. In addition to the gaussfit errors as given in Table 1, we add a 10% systematic error in bands 5 and 4 and 15% in band 3 to account for the calibration uncertainties.

3. Radio Light Curves and Modeling

We present the uGMRT light curves at 1.25, 0.75, and 0.40 GHz in Figure 1 (left panel). The transition from the optically thick to thin regime is seen in the light curves at all frequencies. The peak spectral luminosity at 1.25 GHz is $L_{\nu peak} = 5.3 \times 10^{27}$ erg s^{-1} Hz^{-1}. The spectral indices between 1.25/0.75 GHz and 0.75/0.40 GHz are shown in Figure 1 (right panel). The spectral index α ($F_\nu \propto \nu^\alpha$) in the optically thin regime approaches $\alpha = -0.80 \pm 0.50$ at $t > 400$. The power-law index of the relativistic electron distribution p ($N(E) \propto E^{-p}$) is related to α as $\alpha = -(p-1)/2$, giving $p = 2.60 \pm 1.00$.

We model radio emission from AT 2018cow as synchrotron radiation from a shock created due to the interaction of the

---

Table 1
Details of the uGMRT Observations of AT 2018cow

Date of Observation (UT)	Age (Day)	Frequency (GHz)	Flux Density (μJy)
2018 Jun 27.83	11.39	1.25	<75
2018 Jul 05.83	19.39	1.25	<69
2018 Jul 16.47	30.03	1.25	110 ± 20
2018 Aug 12.71	57.27	1.25	350 ± 82
2018 Sep 07.58	83.14	1.25	810 ± 65
2018 Sep 24.77	100.33	1.25	872 ± 58
2018 Nov 02.26	138.82	1.25	2882 ± 69
2018 Dec 06.77	173.33	1.25	992 ± 34
2019 Feb 04.77	233.33	1.25	882 ± 26
2019 Apr 21.77	309.33	1.25	438 ± 23
2019 Sep 14.77	455.33	1.25	169 ± 20
2020 Jan 06.33	568.89	1.25	93 ± 30
2018 Sep 30.34	105.90	0.75	453 ± 21
2018 Nov 02.42	138.98	0.75	572 ± 19
2018 Dec 08.77	175.33	0.75	755 ± 27
2019 Jan 29.77	227.33	0.75	626 ± 33
2019 Apr 22.77	310.33	0.75	458 ± 35
2019 Sep 14.77	455.33	0.75	303 ± 39
2020 Jan 07.23	569.79	0.75	131 ± 29
2018 Nov 04.39	140.95	0.40	342 ± 70
2018 Dec 07.25	173.81	0.40	518 ± 50
2019 Feb 05.77	234.33	0.40	564 ± 65
2019 Apr 22.77	310.33	0.40	532 ± 65
2019 Sep 14.77	455.33	0.40	410 ± 40
2020 Jan 07.06	569.62	0.40	304 ± 59

Note. The age is calculated assuming 2018 June 16.44 (UT) as the time of event (see Section 1). The listed uncertainties are only statistical uncertainties. There is also a 10%–15% systematic uncertainty (10% for 1.25 and 0.75 GHz flux densities and 15% for 0.40 GHz flux densities) above that.

ejecta with the surrounding medium. Initially the radio emission could be suppressed by free–free absorption (FFA) by the ionized external medium (Chevalier 1982) or synchrotron self-absorption (SSA; Chevalier 1998). The radio flux density, $F(\nu, t)$ in the FFA model is (Chevalier 1982; Weiler et al. 2002)

$$F(\nu, t) = K_1 \left(\frac{\nu}{5\,\text{GHz}}\right)^\alpha \left(\frac{t}{10\,\text{day}}\right)^\beta e^{-\tau_{\text{FFA}}(\nu, t)} \quad (1)$$

$$\tau_{\text{FFA}}(\nu, t) = K_2 \left(\frac{\nu}{5\,\text{GHz}}\right)^{-2.1} \left(\frac{t}{10\,\text{day}}\right)^\delta. \quad (2)$$

Here τ_{FFA} denotes the free–free optical depth and K_1 and K_2 are the flux density and optical depth normalizations, respectively. α, β, and δ denote the spectral and temporal indices of the radio flux densities and temporal index of optical depth, respectively. The radio flux density in the SSA model is (Chevalier 1998; Weiler et al. 2002)

$$F(\nu, t) = K_1 \left(\frac{\nu}{5\,\text{GHz}}\right)^{2.5} \left(\frac{t}{10\,\text{day}}\right)^a (1 - e^{-\tau_{\text{SSA}}(\nu, t)}) \quad (3)$$

$$\tau_{\text{SSA}}(\nu, t) = K_2 \left(\frac{\nu}{5\,\text{GHz}}\right)^{-(p+4)/2} \left(\frac{t}{10\,\text{day}}\right)^{-(a+b)}. \quad (4)$$

Here τ_{SSA} denotes the SSA optical depth. K_1 and K_2 are the flux density and optical depth normalizations, respectively. a
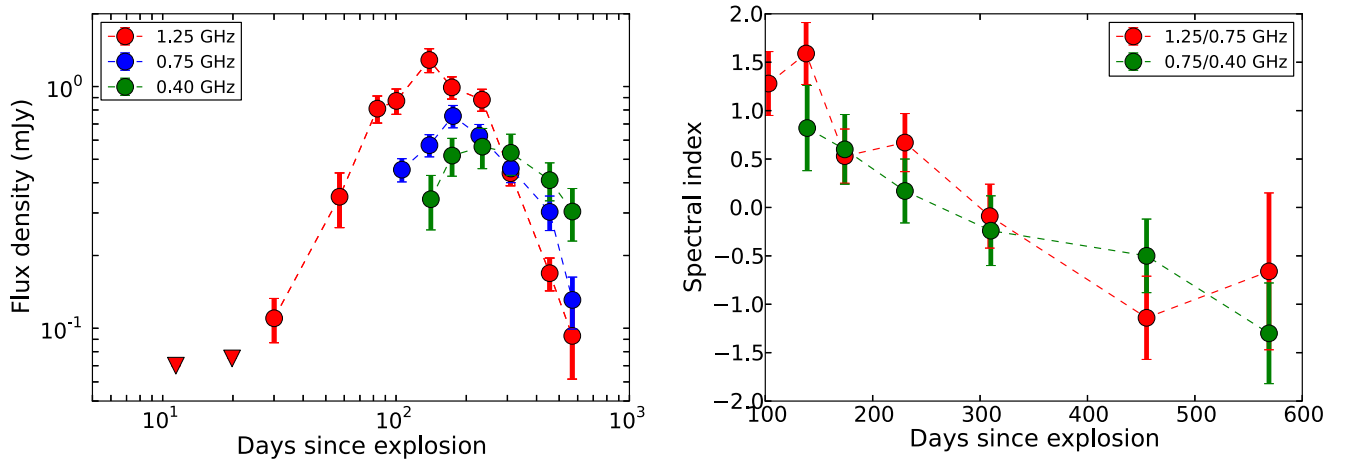
Figure 1. Left panel: the uGMRT light curves of AT 2018cow at 1.25, 0.75, and 0.40 GHz. Right panel: the near simultaneous spectral indices of AT 2018cow between frequencies 1.25/0.75 GHz and 0.75/0.40 GHz at multiple epochs.
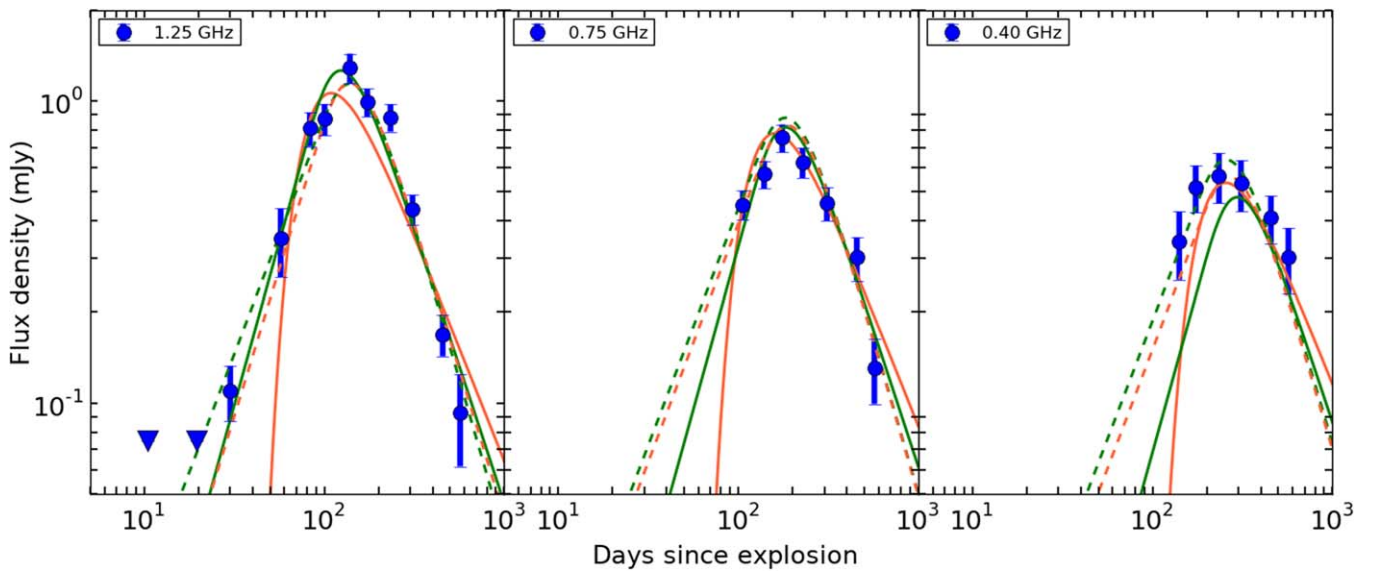

Figure 2. The uGMRT light curves of AT 2018cow at 0.40, 0.75, and 1.25 GHz frequencies. The green and red solid lines denote the best-fit SSA and FFA models, respectively. The green and red dotted lines denote the best-fit inhomogeneous SSA and FFA models, respectively.

and b denote the temporal indices of the flux density in the optically thick and thin phases, respectively.

We perform a combined fit where the data at all ν and t are fit simultaneously with both FFA and SSA models using a chi-square minimization algorithm, curve_fit in python-scipy.[4] K_1, K_2, α, β, and δ are the free parameters in the FFA model and K_1, K_2, a, b, and p are the free parameters in the SSA model. The best-fit models along with the observed data are shown in Figure 2. The best-fit parameters in the FFA model are $K_1 = 32.11 \pm 19.34$, $K_2 = 24.14 \pm 22.98$, $\alpha = -0.53 \pm 0.30$, $\beta = -1.51 \pm 0.21$, and $\delta = -2.81 \pm 0.44$. The best-fit SSA parameters are $K_1 = 0.26 \pm 0.14$, $K_2 = 366.05 \pm 286.71$, $a = 2.16 \pm 0.23$, $b = 1.82 \pm 0.19$, and $p = 2.10 \pm 0.48$. The SSA model gives a better fit to the data ($\chi^2_\nu = 2.6$) than the FFA model ($\chi^2_\nu = 4.7$). The average optically thick spectral index is $\alpha = 1.23 \pm 0.36$, flatter than the standard SSA or FFA values. This can be attributed to the inhomogeneities in the emitting region or CSM (Rybicki & Lightman 1986; Björnsson & Keshavarzi 2017; Weiler et al. 2002; Chandra et al. 2019). In

the FFA model, a clumpy CSM could lead to inhomogeneous absorption and the radio flux density in this case is (Weiler et al. 2002)

$$F(\nu, t) = K_1'\left(\frac{\nu}{5\,\text{GHz}}\right)^{\alpha'}\left(\frac{t}{10\,\text{day}}\right)^{\beta'}\left(\frac{1 - e^{-\tau'_{\text{FFA}}(\nu, t)}}{\tau'_{\text{FFA}}}\right) \quad (5)$$

$$\tau'_{\text{FFA}}(\nu, t) = K_2'\left(\frac{\nu}{5\,\text{GHz}}\right)^{-2.1}\left(\frac{t}{10\,\text{day}}\right)^{\delta'}. \quad (6)$$

K_1' and K_2' denote the flux density and optical depth normalization, respectively. The term $(1 - e^{-\tau'_{\text{FFA}}})/\tau'_{\text{FFA}}$ describes the absorption due to a clumpy CSM where τ'_{FFA} is the FFA optical depth. α', β', and δ' denote the spectral and temporal indices of the radio flux densities and temporal index of optical depth, respectively.

An inhomogeneous synchrotron emitting region can be created due to the inhomogeneous distribution of relativistic electrons and/or magnetic fields. The inhomogeneity can be characterized by a source covering factor, $f_{\text{B,cov}}$, that describes

---

[4] https://docs.scipy.org/doc/scipy/reference/

the variation of the average magnetic field strength over the projected source surface (Björnsson & Keshavarzi 2017). The covering factor gives rise to a range of optical depths over the source and hence broadens the spectrum. $P(B) \propto B^{-a}$ is the probability to find a magnetic field of strength B. $f_{B,cov}$ can be parametrized as $f_{B,cov} \approx f_{B_0,cov}(B/B_0)^{1-a}$, for $B_0 < B < B_1$, where $f_{B_0,cov}$ is the source covering factor for a magnetic field B_0. The observed spectrum will have three regions defined by the synchrotron self-absorption frequency (ν_{abs}); a standard optically thick region where $\nu < \nu_{abs}(B_0)$, a standard optically thin region $\nu > \nu_{abs}(B_1)$, and a transition region where $\nu_{abs}(B_0) < \nu < \nu_{abs}(B_1)$. The radio flux density in the inhomogeneous SSA model is (Björnsson & Keshavarzi 2017; Chandra et al. 2019)

$$F(\nu, t) = K_1'\left(\frac{\nu}{5\,\text{GHz}}\right)^{\alpha''}\left(\frac{t}{10\,\text{day}}\right)^{a'}(1 - e^{-\tau_{SSA}'(\nu,t)}) \quad (7)$$

$$\tau_{SSA}'(\nu, t) = K_2'\left(\frac{\nu}{5\,\text{GHz}}\right)^{-(\alpha''+\frac{p'-1}{2})}\left(\frac{t}{10\,\text{day}}\right)^{-(a'+b')}. \quad (8)$$

Here α'' is the spectral index in the transition region. K_1' and K_2' denote the flux density and optical depth normalization, respectively. In an inhomogeneous model, it is assumed that the locally emitted spectrum is that of the standard synchrotron. However, the inhomogeneities in the magnetic field (B) will give rise to variation in optical depths, and superposition of spectra with varying optical depths will broaden the resulting spectrum. Hence τ_{SSA}' is the effective optical depth coming from the superposition of the spectra of varying optical depths due to different magnetic field in the model. a' and b' denote the temporal index of flux densities in the optically thick and thin phases, respectively, and p' is the power-law index of the electron energy distribution.

We repeat the modeling to account for the effect of inhomogeneities in the FFA (Weiler et al. 2002) and SSA (Björnsson & Keshavarzi 2017; Chandra et al. 2019) models. K_1', K_2', α', β', and δ' are the free parameters in the FFA model and K_1', K_2', a', b', p', and α'' are the free parameters in the SSA model. The fits improve and the SSA model gives a better fit ($\chi_\nu^2 = 0.9$) than the FFA model ($\chi_\nu^2 = 2.0$). The best-fit parameters for the inhomogeneous FFA model are $K_1' = 182.16 \pm 107.56$, $K_2' = 1919.19 \pm 1196.82$, $\alpha' = -0.45 \pm 0.15$, $\beta' = -1.95 \pm 0.19$, and $\delta' = -3.90 \pm 0.21$ and for the inhomogeneous SSA model are $K_1' = 0.16 \pm 0.05$, $K_2' = 1366.26 \pm 989.02$, $a' = 1.57 \pm 0.18$, $b' = 2.07 \pm 0.19$, $p' = 2.33 \pm 0.33$, and $\alpha'' = 1.40 \pm 0.22$. The 1.25, 0.75, and 0.40 GHz light curves of the best-fit model peaks at $t_{peak} = 138, 182$, and 257 days with peak flux densities $F_{peak} = 1.1, 0.9$, and 0.6 mJy, respectively. The peak flux densities are derived by differentiating the best-fit solution to Equations (7) and (8).

3.1. Shock Parameters

The shock radius and magnetic field can be derived from the peak frequency (ν_{peak}) and peak flux density (F_{peak}) of the SSA spectral energy distribution (SED) at a given time (Chevalier 1998). If the emission structure is inhomogeneous, the peak flux density F_{peak} in a standard homogeneous SSA model needs to be replaced with $F_{peak}/f_{B,cov}$ to derive various shock parameters (Björnsson & Keshavarzi 2017). Thus the shock radius (R) and magnetic field (B) values in an inhomogeneous

SSA model can be written as

$$R = R_* \times (f_{B,cov})^{\frac{-p-6}{2p+13}} \quad (9)$$

$$B = B_* \times (f_{B,cov})^{\frac{2}{2p+13}}, \quad (10)$$

where we have defined the shock radius and magnetic field in a standard homogeneous SSA model as R_* and B_*, respectively. R_* and B_* can be expressed using the formulation presented in Chevalier (1998) as,

$$R_* = \left[\frac{6c_6^{p+5}F_{peak}^{p+6}D^{2p+12}}{\left(\frac{\epsilon_e}{\epsilon_B}\right)f(p-2)\pi^{p+5}c_5^{p+6}E_1^{p-2}}\right]^{\frac{1}{(2p+13)}}\left(\frac{\nu_{peak}}{2c_1}\right)^{-1} \quad (11)$$

$$B_* = \left[\frac{36\pi^3 c_5}{\left(\frac{\epsilon_e}{\epsilon_B}\right)^2 f^2(p-2)^2 c_6^3 E_1^{2(p-2)}F_{peak}D^2}\right]^{\frac{2}{(2p+13)}}\left(\frac{\nu_{peak}}{2c_1}\right). \quad (12)$$

In the above equations, ν_{peak} is the peak frequency of the SED at a given time; ϵ_e and ϵ_B denote the fraction of total energy density fed into relativistic electrons and magnetic fields, respectively. D denotes the distance to the source and f is the volume filling factor of the radio-emitting region taken as $f = 0.5$ (Chevalier 1998). However, the dependence of R_* and B_* on f is weak. The value of $c_1 = 6.265 \times 10^{18}$ in CGS units (Chevalier & Fransson 2017). The constants c_5 and c_6 are tabulated for different values of p in Pacholczyk (1970). We use the values corresponding to $p = 2.5$, the closest p value in Pacholczyk (1970) with our best-fit value ($p = 2.33$). E_1 denotes the electron rest mass energy, i.e., 0.51 MeV.

If spatially resolved observations are available, the value of $f_{B,cov}$ can be obtained (Björnsson & Keshavarzi 2017). Since the value of $f_{B,cov}$ is not known for AT 2018cow (although $f_{B,cov} < 1$), we can only estimate R_* and B_* using Equations (9) and (10). Since $f_{B,cov} < 1$, the actual shock radius will be larger than this estimate and magnetic field will be lower than this value. The mean shock velocity between $t = 0$ and a particular age (t) can be estimated as $v = R/t$. However, we can only estimate $v_* = R_*/t$, which is a lower limit to the actual shock velocity.

Following a similar argument as above, the shock internal energy (E) and the mass-loss rate ($\dot{M}$) in an inhomogeneous scenario can be written as

$$E = E_* \times f_{B,cov}^{\frac{-3p-14}{2p+13}} \quad (13)$$

$$\dot{M} = \dot{M}_* \times f_{B,cov}^{\frac{4}{2p+13}}. \quad (14)$$

Here E_* and $\dot{M}_*$ correspond to the shock internal energy and mass-loss rate, respectively, in a standard homogeneous model. The value of E_* can be obtained using the equation derived by Soderberg et al. (2010a).

$$E_* = \frac{1}{\epsilon_B}\left(\frac{B_*^2}{8\pi}\right)\frac{4}{3}\pi R_*^3. \quad (15)$$

Table 2
Shock Parameters of AT 2018cow at Multiple Epochs

Parameters	$\epsilon_B = \epsilon_e = 0.33$			$\epsilon_e = 0.1$, $\epsilon_B = 0.01$		
	Day 138	Day 182	Day 257	Day 138	Day 182	Day 257
R_* ($\times 10^{16}$ cm)	6.12 ± 0.71	9.28 ± 1.07	14.36 ± 1.67	5.38 ± 0.62	8.16 ± 0.95	12.64 ± 1.47
v_* ($\times$c)	0.17 ± 0.02	0.20 ± 0.02	0.21 ± 0.03	0.15 ± 0.02	0.17 ± 0.02	0.19 ± 0.02
B_* ($\times 10^{-1}$Gauss)	1.09 ± 0.03	0.67 ± 0.02	0.37 ± 0.01	0.65 ± 0.02	0.40 ± 0.01	0.22 ± 0.01
E_* ($\times 10^{49}$ erg)	0.08 ± 0.03	0.11 ± 0.04	0.13 ± 0.04	0.67 ± 0.24	0.88 ± 0.31	1.01 ± 0.36
$\dot{M}_*$ ($\times 10^{-5}$ $M_\odot$ yr^{-1})	0.41 ± 0.13	0.27 ± 0.09	0.17 ± 0.05	4.82 ± 1.60	3.15 ± 1.05	1.96 ± 0.65

Note. R_*, B_*, E_*, and $\dot{M}_*$ are the blast-wave radius, magnetic field, shock internal energy, and mass-loss rate defined in Equations (11), (12), (15), and (16), and correspond to values of R, B, E, and $\dot{M}$ for $f_{B,cov} = 1$, i.e., a homogeneous SSA scenario. v_* is the average shock velocity (R_*/t) between $t = 0$ and the listed age under the standard homogeneous assumption.

The $\dot{M}_*$ can be estimated from the magnetic field scaling relation (Chevalier 1998).

$$\frac{B_*^2}{8\pi} = \epsilon_B \frac{\dot{M}_*}{4\pi R_*^2 v_w} v_*^2. \tag{16}$$

We derive the shock parameters assuming equipartition ($\epsilon_e = \epsilon_B = 0.33$) of energy between relativistic electrons and magnetic fields (Soderberg et al. 2010b). While the shock radius and magnetic field are weakly dependent on the equipartition fraction, the shock internal energy and mass-loss rate changes significantly with ϵ_B. We also derive the shock parameters for nonequipartition values $\epsilon_B = 0.01$ and $\epsilon_e = 0.1$ for a comparison.

4. Results and Discussion

We determine R_*, v_*, B_*, E_*, and $\dot{M}_*$ corresponding to $f_{B,cov} = 1$ using Equations (11), (12), (15), and (16). The results are presented in Table 2. The actual R, v, and E will be larger than these values, and B and $\dot{M}$ will be smaller.

4.1. Properties of the Shock

The lower limit on the blast-wave radius is $R_* \sim 6.12 \times 10^{16}$ cm and 14.36×10^{16} cm on $t = 138$ and 257 days post-explosion, respectively. The corresponding lower limit on mean shock velocity at these ages is $v_* \sim 0.2c$. The 3σ upper limit on the shock radius on days 98 and 287 are $R \sim 12.4 \times 10^{16}$ cm and $R \sim 58.4 \times 10^{16}$ cm, respectively, from VLBI observations (Bietenholz et al. 2020). The corresponding upper limits on shock velocity are $v < 0.8c$ and $0.5c$, respectively. Thus the lower limits on shock radius and velocity derived from the uGMRT observations are consistent with the estimates from VLBI observations at similar epochs.

The mean shock velocity up to day 22 is reported as $v \sim 0.13c$ (Ho et al. 2019) and up to day 83 is $v \sim 0.1c$ (Margutti et al. 2019). We estimate the mean shock velocity (using Equation (11)) to be $v \sim 0.14c$ on day 102 from the peak flux density of the 5 GHz light curve (Mohan et al. 2020). The lower limit on shock velocities derived from uGMRT observations are slightly large on $t = 257$ days ($v_* \sim 0.21c$). This marginal increase in shock velocity at later epochs could be indicative of a shock reenergization as it comes out of the dense circumstellar shell, which we discuss in Section 4.2.

The upper limits on the equipartition magnetic fields on days 138, 182, and 257 post-explosion are 0.11, 0.07, and 0.04 G respectively. These are similar to the magnetic fields seen in SNe Ibc (Chevalier & Fransson 2006). The magnetic field strength in the shocked environment is expected to be $B \sim 10^4$ G for models involving a neutron star (Lyutikov & Toonen 2019),

which is significantly higher than the B values derived from our analysis. Thus any scenarios involving a neutron star is less likely to be associated with AT 2018cow.

The lower limit of the shock internal energy during $t = 138$ -257 days is $E_* \sim (0.8-1.3) \times 10^{48}$ erg for $\epsilon_B = \epsilon_e = 0.33$. The energy is sensitive to the choice of ϵ_B value. The lower limit of the shock internal energy increases to $E_* \sim (0.7-1.0) \times 10^{49}$ erg for $\epsilon_B = 0.01$ and $\epsilon_e = 0.1$. The internal energies are comparable to that of most energetic SNe (Soderberg et al. 2010b; Margutti et al. 2019).

4.2. Mass-loss rate

We derive the mass-loss rate of the progenitor in a homogeneous SSA scenario (using Equation 16) to be $\dot{M}_* \sim (4.1-1.7) \times 10^{-6}$ $M_\odot$ yr^{-1} for the shock parameters derived for $t = 138-257$ days. We assume a wind velocity $v_w = 1000$ km s^{-1} and $\epsilon_B = 0.33$. The actual $\dot{M}$ values will be lower than these estimates.

Ho et al. (2019) measure the F_{peak} and ν_{peak} of the SSA spectrum on day 22 post-explosion and estimate the mass-loss rate to be $\dot{M} \sim 4 \times 10^{-4}$ $M_\odot$ yr^{-1} (Ho et al. 2019), two orders of magnitude greater than the $\dot{M}$ derived from uGMRT observations. The mass-loss rates probed by uGMRT observations are at an epoch of stellar evolution 19.3−45.7 yr before the explosion, whereas the $\dot{M}$ derived at $t = 22$ days correspond to ~ 2.2 yr prior explosion (Ho et al. 2019) for the assumed wind velocity. Thus the progenitor of AT 2018cow goes through an enhanced phase of mass-loss close to the explosion. There are pieces of evidence in the literature for a dense shell of medium around AT 2018cow and a possible cutoff in the density distribution from UVOIR (Perley et al. 2019) as well as radio observations (Ho et al. 2019). Ho et al. (2019) constrain the size of the dense CSM shell to be $R \sim 1.7 \times 10^{16}$ cm from the substantial diminishing in the peak flux density of radio spectra. The uGMRT observations probe radii $\gtrsim 6 \times 10^{16}$ cm and are likely probing the material beyond the dense CSM region.

Assuming the surrounding medium to be composed of singly ionized hydrogen, we derive the electron number density $n_e = \frac{\dot{M}}{4\pi r^2 v_w m_p}$. The values of electron number densities are $n_e < 33$ cm^{-3} at radius $R_* > 6.1 \times 10^{16}$ cm. At a radius $R \sim 7 \times 10^{16}$ cm, the n_e of SN 2003bg is ~ 43 cm^{-3} (Soderberg et al. 2006).

5. A Comparison between AT 2018cow with Other Energetic Transients

We compare the radio properties of AT 2018cow with those of other energetic transients in Figure 3. The mean shock velocities in an SSA scenario are plotted as dotted lines (Chevalier 1998).
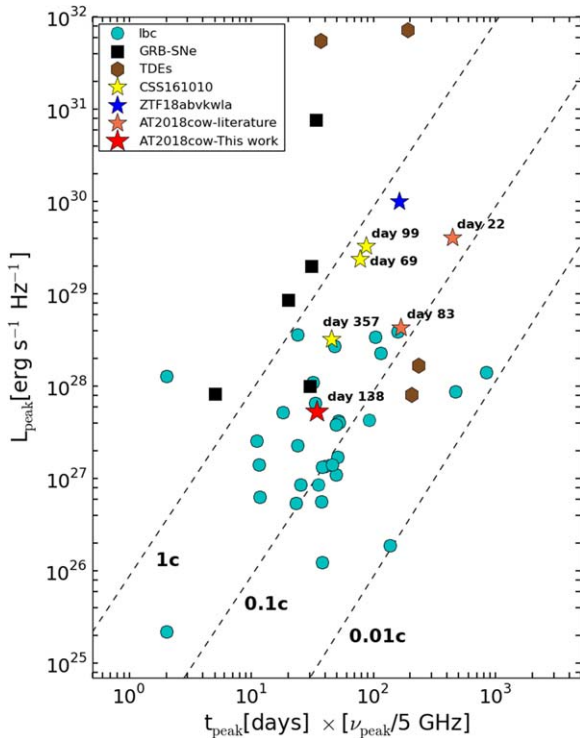
Figure 3. The peak spectral luminosity and peak time of AT 2018cow from uGMRT observations are plotted along with those of other energetic transients. Other FBOTs with radio detections, CSS161010 and ZTF18abvkwla, are also marked for a comparison. The dotted line denotes the mean shock velocity in an SSA scenario. References: Kulkarni et al. (1998); van der Horst et al. (2008); Soderberg et al. (2010b); Zauderer et al. (2011); Berger et al. (2012); Cenko et al. (2012); Margutti et al. (2013, 2019); Alexander et al. (2016, 2017); Chevalier & Fransson (2017); Chandra et al. (2019); Ho et al. (2019); Coppejans et al. (2020); Ho et al. (2020); Nayana & Chandra (2020) and references therein.

While AT 2018cow shows unusually high radio luminosity and peak frequency at early time (day 22; Ho et al. 2019), the peak spectral luminosity of AT 2018cow from the uGMRT observation is comparable to that of other type Ib/c SNe (SNe Ibc) at similar epochs. This indicates that the high L_{peak} and ν_{peak} of AT 2018cow is detected due to the early observation campaign at submillimeter frequencies. Other SNe Ibc could also show high L_{peak} and ν_{peak} had those been observed immediately after the explosion. The peak spectral luminosity of AT 2018cow at $t_{\mathrm{peak}} = 22$ (Ho et al. 2019) and 83 days (Margutti et al. 2019) are also marked in Figure 3 for a comparison. The temporal evolution of AT 2018cow in the L_{peak}–t_{peak} diagram is roughly through a constant velocity line. The shock velocity of AT 2018cow is relatively low compared to those of other FBOTs, $v \geqslant 0.5c$ for CSS161010 (Coppejans et al. 2020) and $v \geqslant 0.3c$ for ZTF18abvkwla (Ho et al. 2020). Coppejans et al. (2020) report evident deceleration in the shock velocity of CSS161010 from $v = 0.55 \pm 0.02c$ to $v = 0.36 \pm 0.04c$ during days 99–357 post-explosion. Such a deceleration is not seen in AT 2018cow up to day 257 post-explosion. The three FBOTs with multiwavelength follow-up observations show diverse properties. A bigger sample of these events will reveal the variety in their intrinsic properties.

6. Summary

We present uGMRT observations of AT 2018cow at 1.25, 0.75, and 0.40 GHz during $11-570$ days post the event. The

peak luminosity at 1.4 GHz is 5.3×10^{27} erg s^{-1} Hz^{-1}. While AT 2018cow shows remarkable luminosity in the submillimeter bands at early times ($t \sim 22$ days; Ho et al. 2019), the luminosity of the transient at late times is very similar to that of energetic SNe Ibc. The uGMRT observations are best represented by a self-absorbed inhomogeneous synchrotron emission model. Assuming the source covering factor to be unity, we estimate the shock radius, magnetic field, mass-loss rate of the progenitor, and shock internal energy. The actual shock radius will be larger and the magnetic field will be smaller than these values since the radio-emitting region is inhomogeneous. The mass-loss rate and energy estimates will also be upper and lower limits, respectively. We derive the lower limit of shock radius to be $R_* \sim (6.12-14.36) \times 10^{16}$ cm during $t = 138-257$ days, consistent with VLBI observations covering similar epochs (Mohan et al. 2020; Bietenholz et al. 2020). The lower limit on the average shock velocity on $t = 257$ day is $v_* \sim 0.21c$ for $\epsilon_{\mathrm{B}} = \epsilon_{\mathrm{e}} = 0.33$ and $v_* \sim 0.19c$ for $\epsilon_{\mathrm{B}} = 0.01$, $\epsilon_{\mathrm{e}} = 0.1$, indicating that the fast-moving ejecta from the event do not experience any deceleration up to $t = 257$ days. The upper limit on the equipartition magnetic field on $t = 138-257$ days is in the range $(0.11-0.04)$ G, much smaller than the expected magnetic field in models involving a neutron star (10^4 G; Lyutikov & Toonen 2019). The upper limit on the mass-loss rate of the progenitor is $\dot{M}_* \sim (4.1-1.7) \times 10^{-6} \, M_\odot$ yr^{-1} for the limits on the shock parameters derived for $t = 138-257$ days, $\sim 10^2$ times lower than the mass-loss rates derived from early ($t = 22$ days) submillimeter observations (Ho et al. 2019). This is consistent with the speculation of a dense circumstellar shell in the vicinity of AT 2018cow (Ho et al. 2019; Perley et al. 2019) if the uGMRT observations are probing the material beyond this dense shell. Our results reveal the importance of low-frequency radio observations to probe the environments of FBOTs at later epochs.

ORCID iDs

Nayana A. J. ⓘ https://orcid.org/0000-0002-8070-5400
Poonam Chandra ⓘ https://orcid.org/0000-0002-0844-6563

References

Alexander, K. D., Berger, E., Guillochon, J., Zauderer, B. A., & Williams, P. K. G. 2016, ApJL, 819, L25
Alexander, K. D., Wieringa, M. H., Berger, E., Saxton, R. D., & Komossa, S. 2017, ApJ, 837, 153
Balberg, S., & Loeb, A. 2011, MNRAS, 414, 1715
Berger, E., Zauderer, A., Pooley, G. G., et al. 2012, ApJ, 748, 36
Bietenholz, M. F., Margutti, R., Coppejans, D., et al. 2020, MNRAS, 491, 4735
Björnsson, C.-I., & Keshavarzi, S. T. 2017, ApJ, 841, 12

Cenko, S. B., Krimm, H. A., Horesh, A., et al. 2012, ApJ, 753, 77
Chandra, P., Nayana, A. J., Björnsson, C.-I., et al. 2019, ApJ, 877, 79
Chevalier, R. A. 1982, ApJ, 259, 302
Chevalier, R. A. 1998, ApJ, 499, 810
Chevalier, R. A., & Fransson, C. 2006, ApJ, 651, 381
Chevalier, R. A., & Fransson, C. 2017, in Handbook of Supernovae, ed. A. Alsabti & P. Murdin (Berlin: Springer), 875
Chevalier, R. A., & Irwin, C. M. 2011, ApJL, 729, L6
Coppejans, D. L., Margutti, R., Terreran, G., et al. 2020, ApJL, 895, L23
Dobie, D., Ravi, V., Ho, A., Kasliwal, M., & Murphy, T. 2018, ATel, 11818, 1
Drout, M. R., Chornock, R., Soderberg, A. M., et al. 2014, ApJ, 794, 23
Fremling, C. 2018, ATel, 11738, 1
Ginzburg, S., & Balberg, S. 2014, ApJ, 780, 18
Ho, A. Y. Q., Perley, D. A., Kulkarni, S. R., et al. 2020, ApJ, 895, 49
Ho, A. Y. Q., Phinney, E. S., Ravi, V., et al. 2019, ApJ, 871, 73
Hotokezaka, K., Kashiyama, K., & Murase, K. 2017, ApJ, 850, 18
Kulkarni, S. R., Frail, D. A., Wieringa, M. H., et al. 1998, Natur, 395, 663
Lyutikov, M., & Toonen, S. 2019, MNRAS, 487, 5618
Margutti, R., Metzger, B. D., Chornock, R., et al. 2019, ApJ, 872, 18
Margutti, R., Soderberg, A. M., Wieringa, M. H., et al. 2013, ApJ, 778, 18
McMullin, J. P., Waters, B., Schiebel, D., Young, W., & Golap, K. 2007, in ASP Conf. Ser. 376, Astronomical Data Analysis Software and Systems XVI, ed. R. A. Shaw, F. Hill, & D. J. Bell (San Francisco, CA: ASP), 127
Metzger, B. D., & Piro, A. L. 2014, MNRAS, 439, 3916
Mohan, P., An, T., & Yang, J. 2020, ApJL, 888, L24
Nayana, A. J., & Chandra, P. 2018, ATel, 11950, 1
Nayana, A. J., & Chandra, P. 2020, MNRAS, 494, 84
Pacholczyk, A. G. 1970, Series of Books in Astronomy and Astrophysics (San Francisco, CA: Freeman)
Perley, D. A., Mazzali, P. A., Yan, L., et al. 2019, MNRAS, 484, 1031
Prentice, S. J., Maguire, K., Smartt, S. J., et al. 2018, ApJL, 865, L3
Pursiainen, M., Childress, M., Smith, M., et al. 2018, MNRAS, 481, 894
Rest, A., Garnavich, P. M., Khatami, D., et al. 2018, NatAs, 2, 307
Rivera Sandoval, L. E., Maccarone, T. J., Corsi, A., et al. 2018, MNRAS, 480, L146
Rybicki, G. B., & Lightman, A. P. 1986, Radiative Processes in Astrophysics (Weinheim: Wiley-VCH)
Smartt, S. J., Clark, P., Smith, K. W., et al. 2018, ATel, 11727, 1
Soderberg, A. M., Brunthaler, A., Nakar, E., Chevalier, R. A., & Bietenholz, M. F. 2010a, ApJ, 725, 922
Soderberg, A. M., Chakraborti, S., Pignata, G., et al. 2010b, Natur, 463, 513
Soderberg, A. M., Chevalier, R. A., Kulkarni, S. R., & Frail, D. A. 2006, ApJ, 651, 1005
Soker, N., Grichener, A., & Gilkis, A. 2019, MNRAS, 484, 4972
Tonry, J. L., Denneau, L., Heinze, A. N., et al. 2018, PASP, 130, 064505
van der Horst, A. J., Kamble, A., Resmi, L., et al. 2008, A&A, 480, 35
Weiler, K. W., Panagia, N., Montes, M. J., et al. 2002, ARA&A, 40, 387
Yu, Y.-W., Zhang, B., & Gao, H. 2013, ApJL, 776, L40
Zauderer, B. A., Berger, E., Soderberg, A. M., et al. 2011, Natur, 476, 425